Evaporative and Radiative Cooling in POST Stratocumulus

H. GERBER

Gerber Scientific, Inc., Reston, Virginia

SZYMON P. MALINOWSKI

University of Warsaw, Warsaw, Poland

HAFLIDI JONSSON

Naval Postgraduate School, Monterey, California

(Manuscript received 14 January 2016, in final form 7 July 2016)

ABSTRACT

Buoyancy reversal by evaporative cooling in entrainment holes has a minimal influence on stratocumulus (Sc) observed during the Physics of Stratocumulus Top (POST) aircraft field study held off the California coast in 2008. High-resolution temperature and microphysics measurements show only small differences for Sc with and without buoyancy reversal predicted by mixing fraction analysis that relates mixtures of cloudy air and free-atmospheric air to buoyancies of the mixtures. The reduction of LWC due to evaporation in the holes is a small percentage (average ~12%) of liquid water diluted in the Sc by entrainment from the entrainment interface layer (EIL) located above unbroken cloud top where most mixing, evaporation, and reduction of the large buoyancy jump between the cloud and free atmosphere occur. Entrainment is dominated by radiative cooling at cloud top.

1. Introduction

Much of the entrainment literature for stratocumulus clouds (Sc) deals with moisture and temperature ''jumps'' across the entrainment interface layer (EIL; also called the inversion) located between the clouds and the free atmosphere (FA). Mixing air from these two sources can cause evaporation of cloud water [liquid water content (LWC)] affecting cloud-top entrainment instability (CTEI; Lilly 1968; Randall 1980; Deardorff 1980) and can determine buoyancy changes associated with mixing fraction analysis (MFA; Nicholls and Turton 1986; Siems et al. 1990) and associated buoyancy reversal (BR). These concepts have been widely used. A selection of related publications includes Albrecht (1991), Wang and Albrecht (1994), Van Zanten and Duynkerke (2002), Stevens et al. (2003), de Roode and Wang (2007), Mellado et al. (2014), and de Lozar and Mellado (2013, 2015a,b). These publications and others describe BR as a potential contribution to buoyancy production and Sc entrainment given specific values of ''jumps.''

Evidence presented by Gerber et al. (2005, 2013) for both DYCOMS II and Physics of Stratocumulus Top (POST) Sc field studies suggested that evaporative cooling and BR were minimal in entrained parcels (called cloud holes in the following), even though BR was predicted for those Sc given observed temperature T and moisture jumps. Further, it was hypothesized that cloud-top detrainment conditioned the EIL with multiple mixing events until a near-buoyancy match was approached near Sc top. At that point, air was entrained into the cloud in a nearly isothermal fashion.

The EIL conditioning was supported by other observations described by Nicholls and Turton (1986) and de Roode and Wang (2007) and was supported from Sc modeling by Kurowski et al. (2009) and Yamaguchi and Randall (2012). Also the direct numerical simulation (DNS) Sc modeling by Delozar and Mellado (2015b) used a null value of the average horizontal buoyancy located at the ''buoyancy inversion point'' located close to the cloud-top boundary above which conditioning occurred.

The present observational study again looks at this cooling and entrainment scenario for Sc from POST and

Corresponding author address: H. Gerber, Gerber Scientific, Inc., 1643 Bentana Way, Reston, VA 20190.
E-mail: hgerber6@comcast.net

DOI: 10.1175/JAS-D-16-0023.1

attempts to quantify how and where cooling and buoyancy changes from evaporating LWC take place in the EIL and in the cloud. BR predictions are tested for Sc with comparisons to observations. A new approach is used where the amount of LWC reduced in holes as a result of evaporation is estimated from effective droplet radius (Re) and droplet concentration measurements from vertical sawtooth profiles centered ±100 m from Sc top. A second approach uses comparisons of high-resolution measurements of T and LWC in holes with cloud unaffected by entrainment. Also used are the recent analyses of the vertical structure of the POST EIL for which two sublayers were identified by Malinowski et al. (2013) and Jen-La Plante et al. (2016).

Time series of LWC, Re, and T for two POST flights (TO6 and TO12), that have the only predicted buoyancy reversal of the POST nighttime flights, are compared to one nighttime flight (TO14) with no predicted buoyancy reversal. Conclusions include the relevance of MFA and BR and give insights on how the entrainment process in the unbroken Sc should be viewed.

2. Aircraft instrumentation

The temperature probe [Modified Ultrafast Thermometer (UFT-M); Kumula et al. 2013] uses resistive wires as sensing elements and operates accurately in and out of cloud. The probe is calibrated by comparison with a Rosemount temperature probe, and it has a resolution of 0.01°C. The UFT-M data rate used is 100 Hz, which corresponds to a ~50-cm in-cloud resolution given the ~50 m s^{-1} airspeed of the Center for Interdisciplinary Remotely-Piloted Aircraft Studies Twin Otter aircraft during cloud penetrations.

The Gerber Particle Volume Monitor (PVM-100A; Gerber et al. 1994) produces integrated values of r^2 and r^3 (r = droplet radius) from droplet spectra proportional to particle surface area (PSA) and LWC, respectively. Re is proportional to the ratio LWC/PSA. LWC has an accuracy of 10% for $r < 18\ \mu$m and a maximum resolution of 0.002 g m^{-3}. Re values are ~15% accurate for $4 < \text{Re} < 12\ \mu$m. The data rate is 100 Hz. The UFT-M and PVM are located near the nose of the aircraft and are separated by ~50 cm.

Droplet concentration is measured by the CAS probe (Droplet Measurement Technologies, Boulder, Colorado) located on the wing of the aircraft. The droplet size range of the probe is 0.5–50-μm diameter, and the data rate is 10 Hz.

3. Buoyancy reversal

BR is predicted by calculating buoyancy b in parcels containing mixtures of cloudy and FT air for the three POST flights using Eqs. (16)–(20) in Stevens (2002) and using observed jumps of T and total water mixing ratio q_t across the EIL listed in Gerber et al. (2013).

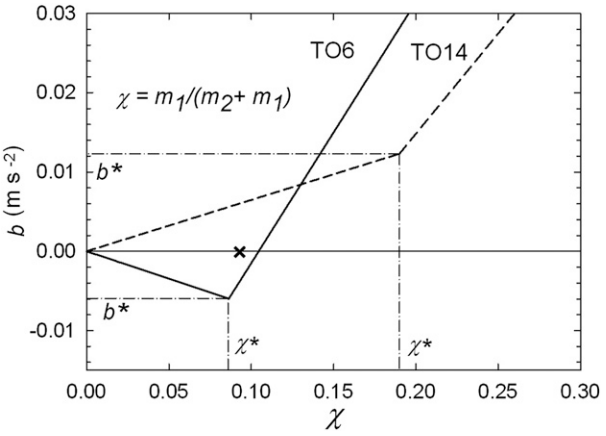

FIG. 1. Predicted mixing curves (MFA) for POST flights TO6 and TO14, where b is the buoyancy of the mixture and χ is the mixing fraction with m_1 the mass of air in the free atmosphere and m_2 the cloud-top air; χ^* and b^* represent the limits where all LWC has evaporated and the air is saturated. The negative b values for TO6 indicate buoyancy instability. The coordinates of χ^* and b^* are given by × for flight TO12.

Figure 1 gives mixing lines, usually referred to as MFA, that combine b with the parcel's mixing fraction χ given by the relative mass of FT air m_1 mixed with a mass of cloudy air m_2; see, for example, Siems et al. (1990) and Van Zanten and Duynkerke (2002). The b^* and χ^* values represent the border where all LWC has evaporated and the air is saturated in the mixture. Figure 1 shows that TO6 has significant predicted buoyancy reversal (negative buoyancy) in mixtures as a result of evaporative cooling for $\chi < \chi^*$. TO14 mixtures have predicted positive buoyancy in mixtures. The mixing lines for TO12 are not included in Fig. 1 given that mixtures for this Sc have $-b^* \sim 0$; the coordinates of χ^* and b^* for TO12 are shown instead by the cross. MFA contains no information on the location where mixing occurs between the cloud and FT.

Another way to look at BR is to calculate the instability criterion for CTEI (Randall 1980; Deardorff 1980). Both TO6 and TO12 have predicted BR given that their instability parameter for CTEI exceeds 0.23. For a discussion of CTEI, see Gerber et al. (2013).

4. Observations

a. Reduced LWC in cloud holes

Figure 2 shows a 50-s part of a sawtooth slant profile with LWC, Re, and T values for TO6 as the aircraft passes up through cloud top. The profile is divided into four layers described by Malinowski et al. (2013)

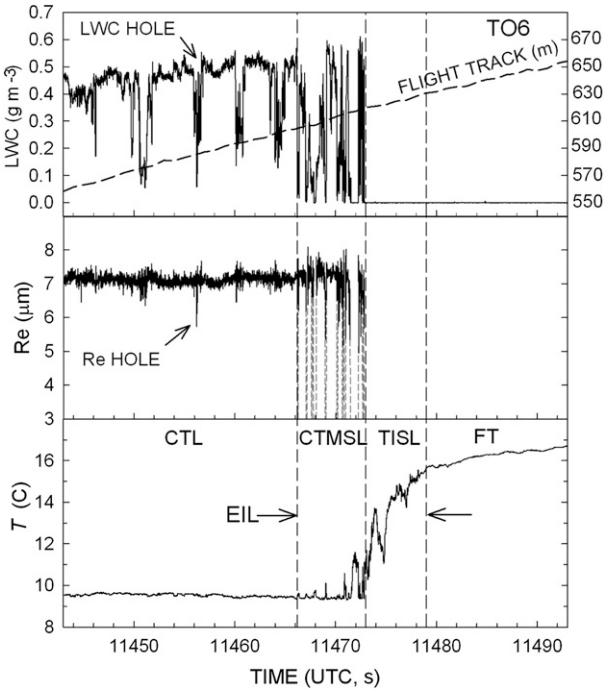

FIG. 2. The ascent (~1.5 m s^{-1}) of the aircraft through the edge of the Sc for flight TO6 showing 100-Hz (top) LWC, (middle) Re, and (bottom) T as a function of time; ~50-cm in-flight resolution. The vertical dashed lines indicate the location of inversion (EIL) sublayers discussed in the text. An example of an "LWC hole" and an "Re hole" is shown. The thin dashed vertical lines in the Re plot indicate where Re goes to zero.

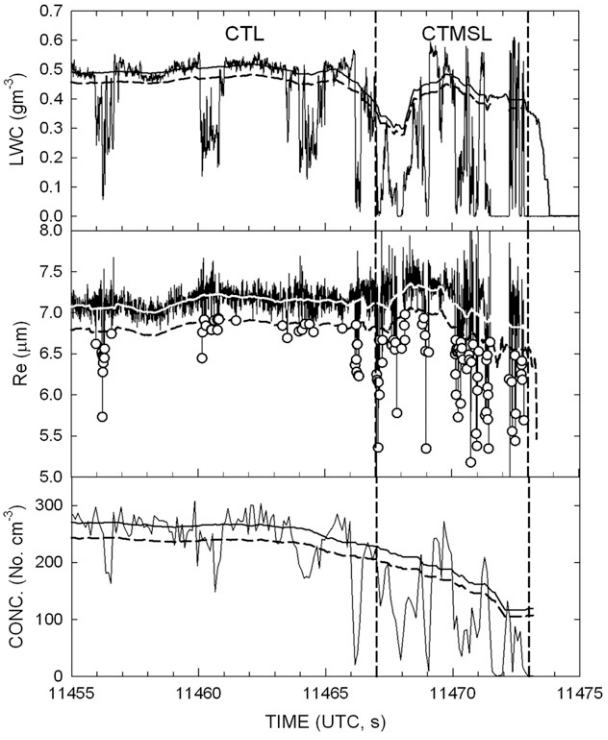

FIG. 3. A smaller interval of the TO6 ascent in Fig. 2 is shown including the time dependence of droplet concentration (CONC). Solid smooth lines are averages of 100-Hz data for LWC and Re and 10-Hz data for CONC. Dashed smooth lines are reduced a fraction from the average lines to minimize the contribution from statistical sampling noise (see text). Open circles are Re data falling below the dashed line. Lines extending to zero values of Re in the CTMSL are not shown.

including the two sublayers in the EIL named cloud-top mixing sublayer (CTMSL) and turbulent inversion sublayer (TISL). CTMSL is described as containing cloudy- and clear-air filaments, T fluctuations as much as 2°C, continuing wind shear, and increased velocity fluctuations in comparison to TISL. TISL is cloud free, has a large T jump, and substantial wind shear and turbulence. Cloud-top layer (CTL) also has large velocity fluctuations, temperature fluctuations typically 0.2°C, and LWC is nearly always $>0\,\mathrm{g\,m^{-3}}$. Holes with LWC $= 0\,\mathrm{g\,m^{-3}}$ occur less than ~0.5% on the average during profiles through the CTL for Sc (Gerber et al. 2013). Here Sc in CTL are defined as "unbroken" by ignoring the few holes without LWC, and unbroken cloud top is chosen as the dividing line between CTL and CTMSL. The vertical dashed lines separating CTL, CTMSL, and TISL in Fig. 2 are fixed by observed LWC values for TO6 and are consistent with the Malinowski et al. (2013) partitioning.

LWC in Fig. 2 shows large variability and Re shows large decreases in CTMSL consistent with water evaporation. The value of T in CTMSL is a maximum of only a few degrees warmer than unbroken cloud and decreases to close to cloud T values at the border between CTL and CTMSL. In CTL LWC shows significant reduction in holes (LWC hole in Fig. 2) defined as having LWC less than the background LWC value and having LWC $> 0\,\mathrm{g\,m^{-3}}$. Figure 2 also shows some reduced values of Re in CTL (Re hole in Fig. 2).

The locations of LWC and Re holes in CTL are correlated as Fig. 2 shows and are better illustrated in Fig. 3, which is an expanded part of Fig. 2. This correlation is also evident in the rest of the TO6 sawtooth profile (not shown). The presence of reduced Re data in LWC holes suggests homogenous mixing where droplets are evaporating causing cooling and BR, while the other and greater amount of data in LWC holes without reduced Re reflects inhomogeneous mixing that may also be a cause of evaporative cooling. In the following the ratio α of reduced LWC in Re holes to the total LWC reduced in holes is estimated.

The aircraft observations show that LWC holes (LWC$_h$) in CTL are sharply defined and are assumed to be caused by entrainment. The slowly varying

TABLE 1. The fraction α of total LWC reduced in the CTL of the Sc due to droplet evaporation. The other parameters from left to right give five-sawtooth-profile averages of total liquid water mass of reduced LWC in entrainment holes and the ratios of droplet concentration N and effective radius (Re^3) in the holes to the same parameters in the cloud unaffected by entrainment [see Eq. (1)]. The numbers in parentheses are one standard deviation of measurement variability.

Flight	$\alpha \times 100$ (%)	$\Sigma_i \Delta LWC_h \times m^3$ (g)	N_h/N_b	Re_h^3/Re_b^3
TO6	15.2 (4.1)	294 (159)	0.586 (0.082)	0.758 (0.038)
TO12	10.5 (2.6)	148 (54)	0.591 (0.097)	0.737 (0.030)
TO14	10.9 (3.4)	396 (94)	0.684 (0.032)	0.768 (0.009)

background LWC (LWC_b) is assumed to be unaffected by entrainment. The desired quantity is the total LWC reduced in the holes for the entire sawtooth profile (~6 km long and a maximum of ~100 m below cloud top) given by $\Sigma_i \Delta LWC_h = \Sigma_i (LWC_h - LWC_b)$, where i represents 100-Hz LWC data. Multiplying both sides of this equation by the unit volume (m^3) gives the total mass (g) of liquid water reduced in the holes over the whole profile. LWC_b is established by using a 400 data point running average of the 100-Hz data and is given by the smooth line in Fig. 3. This average corresponds to a horizontal flight distance of ~200 m that includes holes with lengths encompassing >95% of the entrainment mass flux in Sc as shown in Fig. 6 in Gerber et al. (2013). The procedure described by Gerber et al. (2005) is used to prevent LWC_b from being unduly affected by holes.

A factor $K = 0.94$ is applied to the average curve to give the dashed line in Fig. 3. The value of K is chosen by calculating the amount of mean LWC in the holes times the number of data points in the holes as a function of different values of K. The chosen K value corresponds to the K value where increasing K leads to a rapid increase of that amount as a result of the dashed line starting to intersect the sampling noise of the LWC data caused by the random distribution of ambient droplets.

Also desired is the reduction of LWC in Re holes. This amount can be estimated given that Re ~ r_v (mean volume radius of Sc droplet spectra; Martin et al. 1994) and that $LWC = (4/3)\pi\rho_w N r_v^3$, where ρ_w is water density and N is the droplet concentration. Replacing r_v in the preceding equation with Re permits estimating the total change of ΔLWC_{Re} in Re holes for the whole sawtooth profile:

$$\sum_i \Delta LWC_{Re} \approx \sum_i \left[\left(\frac{N_h Re_h^3}{N_b Re_b^3} - 1 \right) \times LWC_b \right], \quad (1)$$

where the fraction on the right side of Eq. (1) represents the ratio of LWC estimated from Re and N measurements in the holes h to Re and N measured in the background b. The average and the dashed lines for Re and N are determined the same way as for the LWC data; $K = 0.955$ is used for the former and $K = 0.90$ for the latter. Graphical analysis is used to determine values of N_h and N_b for each Re_h data point.

The preceding summations are combined to give

$$\alpha \approx \frac{\sum_i \Delta LWC_{Re}}{\sum_i \Delta LWC_h}, \quad (2)$$

for which the average value is given in Table 1 for five different sawtooth profiles that include 10 penetrations through cloud top for flight TO6.

The same procedure is followed for flights TO12 and TO14 for which five profiles and 10 penetrations were evaluated for each, and the resulting average values are listed in Table 1. (For the ascent of the aircraft for flight TO14, see Fig. 4.) Table 1 also includes average values of the total reduced liquid water mass in the LWC holes and includes average values of N_h/N_b and Re_h^3/Re_b^3. These additions to Table 1 illustrate inherent differences between the three flights. The significantly smaller value of the reduced water mass in holes for TO12 is likely a result of reduced radiative cooling and entrainment caused by a thick layer of water vapor mixing ratio q_v observed above cloud top that had q_v values larger than q_v in the cloud.

The reduced LWC in Re holes can also be used to estimate the mean temperature change $\overline{\Delta T}$ as a result of evaporative cooling in the holes:

$$\overline{\Delta T} \approx 0.5 \frac{\overline{\Delta LWC_{Re}} \times L}{c_p \rho} \approx -0.15°C, \quad (3)$$

where the factor 0.5 is used since evaporative cooling under saturated conditions also leads to some condensation warming (Van Zanten and Duynkerke 2002), overbars indicate mean values, L is the latent heat of evaporation, c_p is the specific heat at constant pressure, and ρ is air density. Individual values of ΔT can be several factors larger than −0.15°C, since ΔLWC_{Re} can range over any fraction of LWC_b.

The values of α in Table 1 are surprisingly similar given the relatively small differences between α for flights TO6 and TO12 with predicted buoyancy reversal

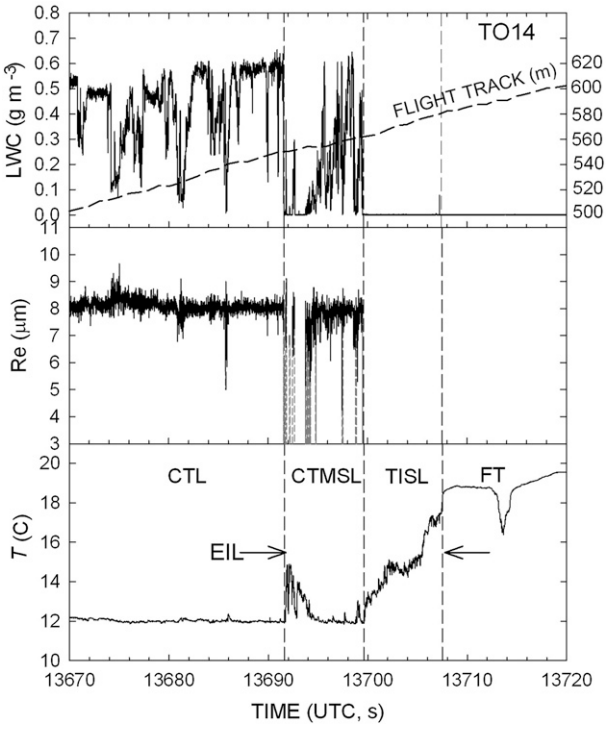

FIG. 4. As in Fig. 2, but for flight TO14.

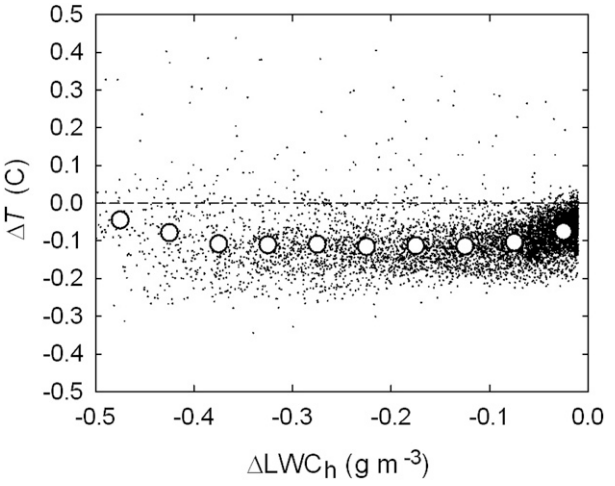

FIG. 5. Flight TO6 differences in temperature ΔT between cloud entrainment holes and the cloud unaffected by entrainment vs the differences for $\Delta\mathrm{LWC}_h$; 50-Hz data. The circles are ΔT averages over 0.05 g m^{-3} $\Delta\mathrm{LWC}_h$ increments.

and for TO14 without predicted reversal. An explanation for the small differences may be a result of turbulence at the border between CTL and CTMSL. Given the strong wind shear and mixing near this border, some warmer parcels may be entrained into the Sc causing evaporation in TO14 holes. This less than solid border may also affect TO6 and TO12 leading to increased uncertainty in their listed values of α. Still, the listed values of α are small, indicating that the reduction of LWC associated with droplet evaporation in Re holes is likewise small.

b. Reduced temperature in cloud holes

A second way to illustrate the role of LWC evaporation in the Sc with predicted buoyancy reversal is to compare direct measurements of LWC in holes ($\Delta\mathrm{LWC}_h$) with the change in temperature ΔT between the holes and the cloud unaffected by entrainment. This again requires conditional sampling of the holes as described in Gerber et al. (2005) and makes use of the fine resolution and accuracy of the UFT-M. Figure 5 shows individual measured data points of $\Delta\mathrm{LWC}_h$ and ΔT from TO6 profiles. The average trend in Fig. 5, given by the circles' data that are averages of ΔT over 0.05 g m^{-3} increments of $\Delta\mathrm{LWC}_h$, shows $\Delta\mathrm{LWC}_h$ nearly independent of ΔT. This trend leads to the conclusion that minimal evaporative cooling occurs in the holes in contrast to the cooling predicted for TO6 by BR.

The trend further suggests that evaporative cooling from inhomogeneous mixing in the holes is minimal, that dilution of LWC in holes is a result of entrainment of air conditioned in the CTMSL, and that radiation cooling is the principal source of cooling shown in Fig. 5.

Cooling due to droplet evaporation determined in section 4a for TO6 should generate some data in Fig. 5, but the data are too infrequent to affect the trend in an obvious visible manner. The average data in Fig. 5 also show some decreasing cooling for larger reductions in $\Delta\mathrm{LWC}_h$ as well as a small number of data points with $\Delta T > 0$°C that may represent entrainment of warmer parcels in keeping with the discussion in section 4a. This behavior is typical of plots resembling Fig. 5 made for most of the other the POST flights (see http://www.gerberscience.com/POSTdata/POSTdata.html). None of the other flights show evidence of BR.

5. Conclusions and discussion

The present analysis is limited to three nighttime POST flights. Two of the flights have predicted buoyancy reversal (BR) due to evaporation of water, and the 3D flight has no predicted BR. The analysis shows that evaporating water and the associated cooling in entrainment holes occurs in the unbroken Sc but is small compared to the reduction of LWC due to dilution of the cloud in the holes. The diluting air comes from the EIL where cloud detrainment conditions the EIL to the point where entrainment into most holes is nearly isothermal.

The cooling in the holes is dominated by longwave flux divergence.

There is only a small difference in the behavior of cooling in the holes regardless of whether BR is or is not predicted for the three POST flights. This is contrary to the prediction of mixing fraction analysis (MFA) that requires all mixtures resulting between the cloud the free troposphere (FT) and containing some remaining LWC to show cooling due to evaporation. It thus can be concluded, assuming the accuracy of the measurements, that for these three flights MFA and BR have little influence on the cooling in entrainment holes.

Details of the physical process causing the limited amount of evaporative cooling in TO6 holes are unclear. A suggested process comes from de Roode and Wang (2007) and Kurowski et al. (2009), who noted that ''local mixing lines,'' rather than the mixing lines' dependence on the whole jumps across the EIL, should be considered that reflect the more frequent mixing near the cloud-top interface for reducing buoyancy to levels permitting entrainment with near-inhomogeneous mixing. Saturation mixture fractions χ^* for such local mixing lines would be much larger than typical values of χ^* found in the literature, and the buoyancy difference b^* due to BR would be much smaller. The location of maximum wind shear and mixing just above cloud top for most POST Sc, and the usually rapid increase of stability in the EIL with height potentially limiting mixing frequency, suggest that ''local mixing lines'' have merit.

Observational reasons may also influence the scarcity of evaporative cooling in TO6 holes including sampling noise in the data as evident in Figs. 2–4. Also, the slower-rate 10-Hz droplet concentration data that corresponds to ~5-m in cloud distance can have an effect; although, entrained holes with lengths approximately less than 5 m include ~90% of the mass entrainment flux in POST Sc (Gerber et al. 2013). In addition, the near independence in TO6 of temperature change in holes from the decrease of LWC in the holes as shown in Fig. 5 supports the rarity of evaporation in holes.

Since only three flights were analyzed here, it is fair to ask how the results apply to Sc in general. The basic characteristic of the POST flights are described in Gerber et al. (2013) with only two nighttime Sc flights with predicted BR, making generalizations difficult for those Sc types. Comparing POST observations to observations from other studies to support the present MFA and BR conclusions is also difficult because of the existence of different types of Sc, of probe choices and location, and of aircraft sampling strategy. An example is the earlier DYCOMS II Sc observational study also off the California coast where Sc were studied ~1000 km downstream of the POST location. The former more mature Sc showed deeper and more numerous LWC-free entrainment holes than such holes for POST Sc, suggesting the possibility that more evaporation occurs in DYCOMS II Sc.

However, some observational and modeling support exists for the present EIL mixing, conditioning, and radiative cooling scenario affecting entrainment holes. The best support comes from Nicholls and Turton (1986), whose Sc conclusions based on observations are close to those of POST. As noted in the introduction, more recent support is found in Gerber et al. (2005, 2013), in the entrainment-parcel-tracking LES modeling by Yamaguchi and Randall (2012), and in the direct numerical simulation (DNS) by de Lozar and Mellado (2015b). Additional support comes from the recent analysis (Jen-La Plante et al. 2016) of POST Sc that shows turbulence responsible for mixing across the TISL and CTMSL is highly anisotropic with eddies elongated in the horizontal and suppressed in the vertical. This again suggests that direct contact between CTL and FT is limited for single mixing events that are required to produce BR as illustrated in Fig. 1.

The study by de Lozar and Mellado (2015b) is of special interest, because DNS resolution as fine as 7.4 cm (de Lozar and Mellado 2013) is used in their studies of DYCOMS II flight RF01. This resolution is finer than the ~50-cm resolution used here; however, the different resolutions should not be important because ~98% of the entrainment mass flux into holes occurs for hole lengths > 1 m [at least in POST Sc; see Fig. 6 in Gerber et al. (2013)].

The RF01 case is also of interest because it is possible to compare the ''efficiency'' of total evaporation in the ''entrainment zone'' from DNS modeling (de Lozar and Mellado 2015b) to TO6 observations. The comparison uses the MFA diagram with TO6 observations to calculate for TO6 an ''efficiency'' of ~0.6 [see Fig. 2 in de Lozar and Mellado (2015b)], which corresponds to ~40% of the evaporation being predicted to occur below the location of the DNS null value of buoyancy. The DNS null value is located at the ''inversion point,'' which sits below the entrainment zone at a horizontal level corresponding to the null value of buoyancy averaged over the Sc field. The de Lozar and Mellado (2015b) results show that modeled cloud top will be found occasionally above as well as below the inversion point level. The null buoyancy value location differs for TO6, since it is located near the border between CTL and CTMSL close to unbroken cloud top, and it can move vertically along with cloud-top motion over the depth of the EIL. The present results differ significantly, showing less evaporation associated with LWC

reduction below the TO6 null buoyancy level. This difference causes uncertainties, not only because the choices of the null buoyancy levels, but also because it deals with two different flights from two different Sc studies, and the DNS study does not include wind shear, whereas TO6 observations show wind shear near cloud top. Further, large vertical changes, such as for radiative cooling and for LWC, can occur over a few vertical meters at Sc cloud top (see for example observations from POST flight TO12; Gerber et al. 2014) so that the vertical variation of Sc top about the average inversion point in DNS may cause different entrainment behavior in comparison to having the buoyancy null value follow cloud top as for TO6.

The complexity of even the unbroken POST Sc is a reminder that more needs to be done to obtain successful entrainment formulation that applies to all Sc. For example, the ''difference method'' equation $w_e = dz_i/dt + w_s$ (Stevens et al. 2003; w_e and w_s are respectively entrainment and subsidence velocities and dz_i/dt is the vertical rate of motion of the inversion base) is not a good framework for characterizing entrainment in POST Sc, with nighttime and daytime Sc showing both positive and negative values of dz_i/dt (see http://www.gerberscience.com/POSTdata/POSTdata.html). It would be useful to quantify the two-way flux of cloud moisture and heat across unbroken Sc cloud top given that such aircraft measurements can be made and compared to model predictions. Wind shear processes need more attention given their effect on the EIL, where the possibility exists that strong directional wind shear can erode cloud top and be a sink of cloud moisture from Sc that advect in a different direction. Moist layers found occasionally above Sc cloud top need better understanding because Sc vertical growth and w_e can be affected.

Future high-resolution observational and modeling studies of Sc should take advantage of the DNS formulations by de Lozar and Mellado. In particular, applying DNS calculations to Sc cloud top rather than their average buoyancy inversion point would provide improved comparisons with aircraft observations. Also, additional application of DNS to Sc without predicted buoyancy reversal such as found for most POST Sc would be useful, given that Sc modeling efforts have focused on Sc with predicted buoyancy reversal as is the case of the oft-studied flight RF01 from DYCOMS II. Observations from RF01 (Fig. 10 of Gerber et al. 2005) show that the hole density for Sc is nearly constant with height for 100 m below cloud top. All the other DYCOMS II flights show the Sc hole density rapidly increasing with height over the 100 m, suggesting that their entrainment behavior may differ.

Acknowledgments. POST was supported by the National Science Foundation and the Office of Naval Research. SPM acknowledges support from the Polish National Science Center (Contract DEC-2013/08/A/ST10/00291).

REFERENCES

Albrecht, B. A., 1991: Fractional cloudiness and cloud-top entrainment instability. *J. Atmos. Sci.*, **48**, 1519–1525, doi:10.1175/1520-0469(1991)048<1519:FCACTE>2.0.CO;2.

Deardorff, J. W., 1980: Cloud top entrainment instability. *J. Atmos. Sci.*, **37**, 561–563, doi:10.1175/1520-0469(1980)037<0131:CTEI>2.0.CO;2.

de Lozar, A., and J. P. Mellado, 2013: Direct numerical simulations of a smoke cloud-top mixing layer as a model for stratocumuli. *J. Atmos. Sci.*, **70**, 2356–2375, doi:10.1175/JAS-D-12-0333.1.

——, and ——, 2015a: Mixing driven by radiative and evaporative cooling at stratocumulus top. *J. Atmos. Sci.*, **72**, 4681–4700, doi:10.1175/JAS-D-15-0087.1.

——, and ——, 2015b: Evaporative cooling amplification of the entrainment velocity in radiatively driven stratocumulus. *Geophys. Res. Lett.*, **42**, 7223–7229, doi:10.1002/2015GL065529.

de Roode, S. R., and Q. Wang, 2007: Do stratocumulus clouds detrain? FIRE I data revisited. *Bound.-Layer Meteor.*, **122**, 479–491, doi:10.1007/s10546-006-9113-1.

Gerber, H., B. G. Arends, and A. S. Ackerman, 1994: New microphysics sensor for aircraft use. *Atmos. Res.*, **31**, 235–252, doi:10.1016/0169-8095(94)90001-9.

——, S. P. Malinowski, J.-L. Brenguier, and F. Burnet, 2005: Holes and entrainment in stratocumulus. *J. Atmos. Sci.*, **62**, 443–459, doi:10.1175/JAS-3399.1.

——, G. Frick, S. P. Malinowski, H. Jonsson, D. Khelif, and S. K. Krueger, 2013: Entrainment rates and microphysics in POST stratocumulus. *J. Geophys. Res. Atmos.*, **118**, 12 094–12 109, doi:10.1002/jgrd.50878.

——, S. P. Malinowski, A. Bucholtz, and T. Thorsen, 2014: Radiative cooling of stratocumulus. *14th Conf. on Atmospheric Radiation*, Boston, MA, Amer. Meteor. Soc., 9.3. [Available online at https://ams.confex.com/ams/14CLOUD14ATRAD/webprogram/Paper248451.html.]

Jen-La Plante, I., and Coauthors, 2016: Physics of Stratocumulus Top (POST): Turbulence characteristics. *Atmos. Phys. Chem.*, **16**, 9711–9725, doi:10.5194/acp-16-9711-2016.

Kumala, W., K. E. Haman, M. K. Kopec, D. Khelif, and S. P. Malinowski, 2013: Modified ultrafast thermometer UFT-M and temperature measurements during Physics of Stratocumulus Top (POST). *Atmos. Meas. Tech.*, **6**, 2043–2054, doi:10.5194/amt-6-2043-2013.

Kurowski, M. J., S. P. Malinowski, and W. W. Grabowski, 2009: A numerical investigation of entrainment and transport within a stratocumulus-topped boundary layer. *Quart. J. Roy. Meteor. Soc.*, **135**, 77–92, doi:10.1002/qj.354.

Lilly, D. K., 1968: Models of cloud-topped mixed layers under a strong inversion. *Quart. J. Roy. Meteor. Soc.*, **94**, 292–309, doi:10.1002/qj.49709440106.

Malinowski, S. P., and Coauthors, 2013: Physics of Stratocumulus Top (POST): Turbulent mixing across capping inversion. *Atmos. Chem. Phys.*, **13**, 15 233–15 269, doi:10.5194/acpd-13-15233-2013.

Martin, G. M., D. W. Johnson, and A. Spice, 1994: The measurement and parameterization of effective radius of droplets in warm stratocumulus clouds. *J. Atmos. Sci.*, **51**, 1823–1842, doi:10.1175/1520-0469(1994)051<1823:TMAPOE>2.0.CO;2.

Mellado, J. P., B. Stevens, and H. Schmidt, 2014: Wind shear and buoyancy reversal at the top of stratocumulus. *J. Atmos. Sci.*, **71**, 1040–1057, doi:10.1175/JAS-D-13-0189.1.

Nicholls, S., and J. D. Turton, 1986: An observational study of the structure of stratiform cloud sheets: Part II. Entrainment. *Quart. J. Roy. Meteor. Soc.*, **112**, 461–480, doi:10.1002/qj.49711247210.

Randall, D. A., 1980: Conditional stability of the first kind upside down. *J. Atmos. Sci.*, **37**, 125–130, doi:10.1175/1520-0469(1980)037<0125:CIOTFK>2.0.CO;2.

Siems, S. T., C. S. Bretherton, M. B. Baker, S. Shy, and R. E. Breidenthal, 1990: Buoyancy reversal and cloud-top entrainment instability. *Quart. J. Roy. Meteor. Soc.*, **116**, 705–739, doi:10.1002/qj.49711649309.

Stevens, B., 2002: Entrainment in stratocumulus topped mixed layers. *Quart. J. Roy. Meteor. Soc.*, **128**, 2663–2690, doi:10.1256/qj.01.202.

——, and Coauthors, 2003: On entrainment rates in nocturnal marine stratocumulus. *Quart. J. Roy. Meteor. Soc.*, **129**, 3469–3493, doi:10.1256/qj.02.202.

Van Zanten, M. C., and P. G. Duynkerke, 2002: Radiative and evaporative cooling in the entrainment zone of stratocumulus—The role of longwave radiative cooling above cloud top. *Bound.-Layer Meteor.*, **102**, 253–280, doi:10.1023/A:1013129713315.

Wang, Q., and B. A. Albrecht, 1994: Observations of cloud-top entrainment in marine stratocumulus clouds. *J. Atmos. Sci.*, **51**, 1530–1547, doi:10.1175/1520-0469(1994)051<1530:OOCTEI>2.0.CO;2.

Yamaguchi, T., and D. A. Randall, 2012: Cooling of entrained parcels in a large-eddy simulation. *J. Atmos. Sci.*, **69**, 1118–1136, doi:10.1175/JAS-D-11-080.1.